

Article

FENGYUN-4A Advanced Geosynchronous Radiation Imager Layered Precipitable Water Vapor Products' Comprehensive Evaluation Based on Quality Control System

Yong Zhang ^{1,*} , Jun Li ¹, Zhenglong Li ², Jing Zheng ¹, Danqing Wu ³ and Hongyu Zhao ³

¹ National Meteorological Satellite Center, China Meteorological Administration, Beijing 100081, China; jun.li@cma.gov.cn (J.L.); zhengjing@cma.gov.cn (J.Z.)

² Cooperative Institute for Meteorological Satellite Studies, University of Wisconsin-Madison, 1225 West Dayton Street, Madison, WI 53706, USA; zli@ssec.wisc.edu

³ Beijing PIESAT Information Technology Co., Ltd., Beijing 100093, China; wudanqin@piesat.cn (D.W.); zhaohongyu@piesat.cn (H.Z.)

* Correspondence: zhangyong@cma.gov.cn; Tel./Fax: +86-10-6840-9402

Abstract: A physical retrieval algorithm has been developed for deriving the layered precipitable water vapor (LPWs) product from infrared radiances of the Advanced Geosynchronous Radiation Imager (AGRI) onboard FengYun-4A (FY-4A), the first of the new generation of Chinese geostationary weather satellites (FengYun-4, or FY-4 Series). The FY-4A AGRI LPWs are evaluated with different types of reference datasets based on Quality Control System (QCS), including those from Himawari-8 AHI (Advanced Himawari Imager), MODIS (Moderate Resolution Imaging Spectroradiometer), Radiosonde, ERA5 (European Centre for Medium-Range Weather Forecasts Reanalysis v5), NCEP (National Centers for Environmental Prediction) reanalysis and CMA (China Meteorological Administration) forecast product from global medium range numerical weather prediction (NWP) system. QCS is one of the important components of FY-4A ground segment, which mainly focuses on the satellite products' evaluation and validation. It is found that the AGRI LPW product has a good agreement with different evaluating sources and the quality is favorable and stable. With the capability of frequent (5-min interval) observations over the East Asia and Western Pacific regions, the AGRI LPW products can be used to investigate the atmospheric temporal and spatial variations in the pre-landfall environment for typhoons. The QCS is a useful tool to monitor, evaluate, and validate the AGRI LPW products.

Keywords: FengYun-4 (FY-4) Geostationary Satellite; Advanced Geosynchronous Radiation Imager (AGRI); layered precipitable water vapor (LPW); retrieval; evaluation; Quality Control System (QCS)



Citation: Zhang, Y.; Li, J.; Li, Z.; Zheng, J.; Wu, D.; Zhao, H. FENGYUN-4A Advanced Geosynchronous Radiation Imager Layered Precipitable Water Vapor Products' Comprehensive Evaluation Based on Quality Control System. *Atmosphere* **2022**, *13*, 290. <https://doi.org/10.3390/atmos13020290>

Academic Editor: Yong Chen

Received: 29 December 2021

Accepted: 3 February 2022

Published: 9 February 2022

Publisher's Note: MDPI stays neutral with regard to jurisdictional claims in published maps and institutional affiliations.



Copyright: © 2022 by the authors. Licensee MDPI, Basel, Switzerland. This article is an open access article distributed under the terms and conditions of the Creative Commons Attribution (CC BY) license (<https://creativecommons.org/licenses/by/4.0/>).

1. Introduction

Fengyun-4 (FY-4) is the latest generation of China's geostationary meteorological satellites for high-impact weather (HIW) event monitoring, warning, and forecasting, with the first FY-4A launched on 11 December 2016 [1]. Compared with the existing operational FY-2 series, the FY-4 series have a longer operating lifetime and improved capabilities for weather and environmental monitoring, including a new capability for vertical temperature and moisture sounding of the atmosphere with its high-spectral-resolution infrared (IR) sounder, the Geostationary Interferometric Infrared Sounder (GIIRS). For the coming 15 years, the three-axis stabilized FY-4 series will offer the imaging capabilities with full-disc coverage every 15 min or better, and the option for more rapid regional and mesoscale observation modes. FY-4 represents an unprecedented expansion in China's geostationary remote sensing capabilities. FY-4A is experimental, and the subsequent satellites in the FY-4 series will be operational. The remaining satellites of this series are planned to be launched in the near future with FY-4B launched in 2021 [2]. For the FY-4 operational

series of satellites, the main observation capabilities are similar to those onboard the FY-4A, with some significant performance improvements, such as more observation channels, finer spatial resolution, and higher observing frequency of the Advanced Geosynchronous Radiation Imager (AGRI) and GIIRS. FY-4 series will improve most products of FY-2 series and introduce many new products, such as atmospheric temperature and moisture profiles, atmospheric instability indices, layer precipitable water vapor (LPW), rapid developing clouds, and others [1,3]. These improved and new capabilities allow better weather and environmental applications.

As one of the main payloads onboard FY-4A, AGRI has 14 spectral bands that are quantized with 12 bits per pixel and sampled at 1 km at nadir in the visible (VIS), 2 km in the near-infrared (NIR), and 4 km in the remaining IR spectral bands. Besides the increased number of spectral bands, the FY-4A AGRI represents an improvement of the existing FY-2 visible and infrared spin-scan radiometer (VISSR) in almost all other aspects, including increased spectral resolution, improved radiometric accuracy, and improved imager registration and navigation. Table 1 summarizes the FY-4A AGRI spectral bands, along with the spatial resolution, the signal-to-noise specification, and the associated main applications. The AGRI spectral bands will enable generation of new products and refinement of existing products of FY-2. AGRI’s imaging capability is comparable or close to other advanced imagers, such as the new generation of U.S. Geostationary Operational Environmental Satellite (GOES-R series) Advanced Baseline Imager (ABI) [4,5] and the European Meteosat Third Generation (MTG) Flexible Combined Imager (FCI) [6], as well as other similar instruments on board geostationary meteorological satellites.

Table 1. Specifications for AGRI on board FY-4A.

Spectral Coverage	Spectral Band (μm)	Spatial Resolution (km)	Sensitivity	Main Applications
VIS/NIR	0.45–0.49	1	S/N * ≥ 90 (ρ ** = 100%)	Aerosol, visibility
	0.55–0.75	0.5	S/N ≥ 150 (ρ = 100%)	Fog, clouds
	0.75–0.90	1	S/N ≥ 200 (ρ = 100%)	Aerosol, vegetation
	1.36–1.39	2	S/N ≥ 150 (ρ = 100%)	Cirrus
	1.58–1.64	2	S/N ≥ 200 (ρ = 100%)	Cloud, snow
	2.10–2.35	2	S/N ≥ 200 (ρ = 100%)	Cloud phase, aerosol, vegetation
	3.50–4.00	2	NEΔT *** ≤ 0.7 K (300 K)	Clouds, fire, moisture, snow
	3.50–4.00	4	NEΔT ≤ 0.2 K (300 K)	Land surface
Midwave IR	5.8–6.7	4	NEΔT ≤ 0.3 K (260 K)	Upper-level WV
	6.9–7.3	4	NEΔT ≤ 0.3 K (260 K)	Midlevel WV
Longwave IR	8.0–9.0	4	NEΔT ≤ 0.2 K (300 K)	Volcanic ash, cloud-top phase
	10.3–11.3	4	NEΔT ≤ 0.2 K (300 K)	SST, LST
	11.5–12.5	4	NEΔT ≤ 0.2 K (300 K)	Clouds, low-level WV
	13.2–13.8	4	NEΔT ≤ 0.5 K (300 K)	Clouds, air temperature

* S/N is signal to noise ratio. ** ρ is typical reflectance. *** NEΔT is noise equivalent temperature difference.

The products from AGRI of FY-4C and after will have an IR spatial resolution of 2 km, together with those from other international geostationary satellites, will provide near global quantitative datasets with high spatial and temporal resolutions for weather and climate applications.

The FY-4A geostationary ground segment consists of: Data Transmission System (DTS), Mission management and Control System (MCS), Navigation and Registration System (NRS), Calibration and Validation System (CVS), Product Generation System (PGS), Space Weather System (SWS), Quality Control System (QCS), Data Service System (DSS) and Application Demonstration System (ADS), etc.

Atmospheric precipitable water vapor plays an important role on the Earth’s weather and climate, especially under the global warming condition. It not only affects the radiation

balance and atmospheric circulation, but also impacts the intensity of precipitation by changing the moisture transport. The atmospheric water vapor content is an important parameter for weather forecasting, a key factor for studying the global water cycle, climate change, the energy circulation of the earth-atmosphere system, and the input parameters for aerosol and surface temperature retrieval [7–9]. Water vapor is an important factor in climate as the main feedback factor associated with the radiation effect and moisture dynamics [10]. It is the most abundant greenhouse gas, and the increase of tropospheric water vapor is closely related to climate warming [7]. Therefore, accurate estimate of atmospheric water vapor content is important towards the predictability of rainfall and our understanding of many feedback processes.

Over the past few decades, many techniques have been developed to obtain atmospheric precipitable water vapor (PW), or the vertically integrated water vapor content, including in situ measurements from radiosonde observation (RAOBs) [11], retrievals from ground-based sun photometry [12], microwave radiometers [13–15], Raman radar [16,17], Global Positioning System (GPS) receivers [18–20], and satellite remote sensing [21,22]. Among them, in situ radiosonde represents the most traditional PW measurement technology. Because the radiosonde can obtain PW with controlled accuracy, it is widely used as the reference database to evaluate other PW retrieval techniques [23,24]. But limitations such as high cost, sparse spatial distribution, large bias in the upper troposphere, and low temporal and spatial resolution (launched only twice a day) prevent the usability of radiosonde for monitoring the wide range of weather process and short-term weather forecasting. Ground-based GPS, ground-based sun photometer and microwave radiometers measurements are three kinds of reliable and common techniques to retrieve PW with high precision and accuracy as well as high temporal resolution. However, these ground-based observations are still fairly sparse for most areas.

Satellite observations can be used as a more effective technology to monitor the spatial distribution and temporal changes of PW on a large scale. For example, the MODerate resolution Imaging Spectroradiometer (MODIS) onboard TERRA and AQUA provides PW observations with high spatial resolution [25–28]. Over the past 20 years, the MODIS PW products have been extensively evaluated using ground-based PW observations over most areas of the world [29–34], and used in weather, climate, and hydrological cycle studies [26,28,31]. Other satellite-based PW products include those from Atmospheric InfraRed Sounder (AIRS), Cross-track Infrared Sounder (CrIS), and Infrared Atmospheric Sounding Interferometer (IASI) [35]. Due to low spatial and temporal resolutions of low earth orbit (LEO) satellites, there are about 50% data missing over high-altitude area (i.e., Tibetan Plateau) from $0.05^\circ \times 0.05^\circ$ spatial resolution of MODIS data [36]. In addition, measurements from sounders with coarser spatial resolution have limited capability on detecting small scale atmospheric moisture spatial variations [37].

Compared with LEO based PW products, geostationary orbit (GEO) offers the unique value with much higher temporal resolution. For example, the ABI onboard the new generation GOES-16/-17 satellite has fine temporal (30 s to 10 min) and spatial resolutions (0.5–2 km), and 16 spectral bands. GOES-16 started a new era for the U.S. geostationary satellite observing system. However, due to the lack of an infrared sounder on the spacecraft, the ABI is used to continue the legacy atmospheric profile (LAP) products [4] that the previous GOES Sounder [38] provided for nowcasting and weather forecasting [39]. Those LAP products from ABI include the legacy atmospheric vertical moisture profile (LVM), legacy atmospheric vertical temperature profile (LVT), total precipitable water (TPW), layered precipitable water (LPW), and derived atmospheric stability indices (DSI) over each 5×5 ABI pixels box area with clear-sky IR band radiances [40]. The GOES-R LAP products have been evaluated by National Weather Service (NWS) forecasters at the NOAA Hazardous Weather Testbed (HWT) and received positive feedbacks for severe storm nowcasting and forecasting.

The LPW product retrieval algorithm for FY-4 AGRI was introduced in Zhang et al. (2019) [41]. The algorithm is similar to that used for the operational GOES Sounder profile

retrieval [42] and is responsible for the retrieval of atmospheric layer integrated moisture for AGRI field of regard (FOR) (an $M \times M$ pixel box). The product generation takes IR brightness temperatures (BTs) from all AGRI IR channels as inputs along with numerical weather prediction (NWP) forecast output as background. The one-dimensional variational (1Dvar) based physical retrieval algorithm modifies the temperature and moisture profiles based on the differences between the observed and the calculated BTs using Newton's nonlinear iterative method [43]. The LPW products are derived from the moisture profile retrievals, including TPW and PW at three atmospheric layers. TPW is the amount of liquid water (in the unit of cm) if all the atmospheric water vapors in the column was condensed. Layer perceptible water (LPW) provides information on the water vapor contained in a vertical column of unit cross-section area in three layers in the troposphere in sigma coordinate: LPW low (LPWL): 0.9–surface (SFC), LPW middle (LPWM): 0.7–0.9, LPW high (LPWH): 0.3–0.7. The FY-4A AGRI clear sky LPW products are available in 12 km resolution (an FOR of a 3×3 box area) for full-disc or China region.

It is important to point out that GIIRS is the primary instrument to provide water vapor (and temperature) profile information with its thousands of sounding channels. However, comparing to AGRI, there are several limitations in the FY-4A GIIRS water vapor products for nowcasting and forecasting, including spatial coverage, temporal and spatial resolutions. AGRI covers different sectors including full disc, north hemisphere, China area and focus domains, while GIIRS only covers the rectangle area of 3°N – 55°N and 60°E – 137°E . AGRI has a temporal resolution better than 15 min, much better than GIIRS' 2 h. While the spatial resolution of AGRI LPW products is 12 km, comparable to GIIRS' 16km, the AGRI LPW products have better retrieval yields than what would have been achieved from GIIRS. This is because AGRI retrievals are performed if there are less than 9 cloudy IR pixels within an FOR. Such higher temporal and spatial resolution data are important in the climate sensitive regions such as the high-altitude mountain terrain region of Tibetan Plateau in particular where there is limited number of ground-based observations [44]. It should be noted that both spatial and temporal resolutions will be improved for moisture soundings from the future Fengyun-4 GIIRS measurements.

Comprehensive evaluation of FY-4A AGRI LPW products has been carried out and the results are presented in this paper. Section 2 describes the data used for comparisons in this study. Section 3 introduces the Quality Control System of FY-4A ground segment. Section 4 explains the evaluating method. And Section 5 presents results and discussions, followed by conclusions in Section 6.

2. Data

To evaluate FY-4A AGRI LPW products, different types of water vapor data were collected, compared and analyzed, including Himawari-8 AHI Layered Perceptible Water data, RAOB data, ECMWF Reanalysis v5 (ERA5) data, National Centers for Environmental Prediction (NCEP) reanalysis, and China Meteorological Administration (CMA) forecast product from NWP system. Brief introductions of these data are shown below.

2.1. FY-4A AGRI LPW Product

The AGRI can complete a full disk scan every 13 min, a regional scan covering China every 5 min, and a meso scan every 2 min. To reduce temporal redundancy and balance between the full disks, regional, and meso scans, the AGRI is configured to have 40 full disks and 165 China regional LPWs files for each day. The full disk observations are made every nominal hour plus 15 min before and after the nominal 3-h (00, 03, 06, etc.), which is specially designed for atmospheric motion vector (AMV) applications. Three consecutive regional observations (also for AMV) are made at 30 min after every nominal hour and 15 min before and after nominal hour when there are no full disc observations [1]. Since 18 January 2019, LPW products of FY-4A are publicly available. The data used in this study are from the time period from 23 October 2019 to 30 May 2020 from the domains of full disk and China region.

2.2. Himawari-8 AHI LPW Data

The AHI LPW retrievals are also based on the operational GOES Sounder profile retrieval algorithm [42], which is a 1Dvar retrieval method based on optimal estimation theory [40,45]. The Quasi-Newton iteration technique is employed in the 1Dvar solution, and the University of Wisconsin-Madison's (USA) SeeBor emissivity database is applied as a prescribed input [46]. Since the IR bands of AHI are similar to those of ABI [4], the employed bands are also the same as those of the ABI. After the atmospheric temperature and moisture profiles have been retrieved, the derived products are calculated from the profiles, and the methods for obtaining these products are described in the ABI/GOES-R legacy atmospheric profile (LAP) retrieval Algorithm Theoretic Basis Document (ATBD) [47]. The LAP retrieval algorithm [43,45] has been tested and validated using the spinning enhanced Visible and Infrared Imager (SEVIRI) and the GOES Sounder as proxy [48], as well as the AHI [49] and ABI [40] observations. While the LPWs are not operational LAP products, they can be calculated from the retrieved moisture profiles using the same definition of the three layers in sigma coordinates. The AGRI LPWs will be inter-compared with those from AHI to ensure comparable quality from the two satellites.

2.3. MODIS PW Product

The MODIS Precipitable Water product consists of column water-vapor amounts. During the daytime, a near-infrared algorithm is applied over clear land areas of the globe and above clouds over both land and ocean. Over clear ocean areas, water-vapor estimates are provided over the extended glint area. An infrared algorithm for deriving atmospheric profiles is also applied both day and night for Level 2. There are two MODIS Water Vapor data product files: MOD05, containing data collected from the Terra platform; and MYD05, containing data collected from the Aqua platform. The Level 2 data are generated at the 1-km spatial resolution of the MODIS instrument using the near-infrared algorithm during the day, and at 5-km resolution (a 5×5 box) both day and night using the infrared algorithm when at least nine FOVs are cloud free. The infrared-derived precipitable water vapor is generated as one component of product MOD07/MYD07, and simply added to product MOD05/MYD05 for convenience. The solar retrieval algorithm relies on observations of water-vapor attenuation of reflected solar radiation in the near-infrared MODIS channels so that the product is produced only over areas where there is a reflective surface in the near IR [25–28].

2.4. RAOB Data

There are two RAOB datasets used in this study. For FY-4A AGRI China region, the RAOB data was obtained by the L-band sounding system (1675 MHz) of the CMA, named as "soundings", and those collected from the University of Wyoming website [50] were named as TK. It contains the observation data of the height, temperature, dew point temperature, wind direction, wind speed of the 89 Chinese radiosonde observation stations obtained by the National Meteorological Information Center (NMIC) through the domestic communication system of China. All these stations only cover Chinese territory. The CMA sounding system is composed of Global Telecommunications System-1 (GTS1) digital electronic radiosonde, secondary wind-finding radar and a ground-check set. It is widely used to measure the air pressure, temperature, relative humidity, and wind from the ground to about 30 km at radiosonde sites across China. The accuracy of the measured pressure, temperature, and relative humidity is 1–2 hPa, 0.2–0.3 °C and 4–5%, respectively [51]. The radiosonde LPW was derived by integrating the specific humidity using the same algorithm for AGRI with the RAOB observed surface pressure. The RAOB LPW will be used as reference for the evaluation purpose at 00 and 12 UTCs.

2.5. ERA5 Reanalysis Data

ERA5 is the fifth generation ECMWF atmospheric reanalysis [52]. The ERA5 was produced using the 4D-Var data assimilation in CY41R2 of ECMWF's Integrated Fore-

cast System (IFS), with 137 hybrid sigma/pressure (model) levels in the vertical, with the top level at 0.01 hPa. The ERA5 is preferred over the previously widely used ECMWF Re-analysis Interim (ERA-Interim), which is the third-generation global atmospheric re-analysis from ECMWF [53], because of higher temporal resolution of 1 h and higher spatial resolution of 31 km. The ERA5 complements the RAOB measurements in both time and space, making it possible to evaluate satellite sounding products on extended spatial and temporal scales.

2.6. NCEP Data

The NCEP/NCAR Reanalysis project uses a state-of-art analysis/forecast system to perform data assimilation using past data from 1948 to the present [54]. A large subset of this data is available from Physical Sciences Laboratory (PSL) in its original 4 times daily format and as daily averages. The local ingestion process took only the 0 Z, 6 Z, 12 Z, and 18 Z reanalyzed values. Those four times were used to make the daily time series and monthly means in this study.

2.7. CMA T639 Products

T639L60 global medium range NWP model products have high resolutions [51]. Its global horizontal resolution reaches 30 km with 60 vertical layers, and its model top reaches 0.1 hPa. The analysis data of T639 were used in this paper. The data files adopt grib2 format, which are disseminated daily at 00:00 and 12:00 UTC.

3. Quality Control System of FY-4A Ground Segment

Quantitative remote sensing products' quality evaluation and validation is an important part of the FY-4A ground segment and the basic technical goal of the product quality control system. Satellite remote sensing products are derived by processing the data obtained by satellite remote sensors through scientific methods. The quality of the products directly affects the quantitative applications of remote sensing data. In high-altitude and mountain terrain areas, especially when the estimated parameters are of the same order with the measurement uncertainties, maintaining quality control of satellite retrieval products are important [44]. It is very necessary to carry out the evaluation and validation of the accuracy of satellite remote sensing products. An operational processing system for products quality control, named QCS of FY-4A, has been developed.

4. Method

In this study, the temperature and humidity profiles of RAOB data, the layer water vapor products of Himawari-8 AHI, NCEP, T639, ERA5, and TPW of Aqua/Terra MODIS are used to calculate bias, standard deviation (STD), root mean square error (RMSE) and correlation coefficient (CC). These indicators will be used to characterize the quality of the FY-4A AGRI LWP products.

Because the spatial resolution and observing time of the AGRI LPW products and the reference evaluation data are different, according to their own characteristics, appropriate methods are needed to do the spatial and time matching, which will be introduced later. After data preprocessing and matching, the FY-4A AGRI LPW products are compared with the reference datasets for evaluation. Some statistical indicators will be calculated. This will be done for different latitudes, different time periods, and user-defined regions. Finally, the visualization of the evaluation results of various statistical indicators are shown in the form of geographical distribution maps, histograms, and statistical tables.

4.1. Temporal Matching

The radiosonde data is obtained twice a day (0:00 and 12:00 UTC). Based on the observation time of the RAOB data, the time matching threshold is set to ± 60 min, and the nearest FY-4A AGRI LPW products within the time interval is searched for matching the RAOB data. The time resolution of Himawari-8 AHI LPW data is 10 min. Based on

the observation time of Himawari-8 AHI LPW data, the time matching threshold is set to ± 5 min, and the nearest FY-4A AGRI LPW product within the time interval is selected for matching. For TERRA/AQUA MODIS PW data, also based on the observation time of MOIDS, the time interval is set to ± 5 min, and the nearest FY-4A AGRI LPW product within the time interval is selected. The global model water vapor profile data (include ERA-5, NCEP and T639 data) is generally generated 4 times a day (0 Z, 6 Z, 12 Z, and 18 Z) except ERA-5. Based on the generation time of the model data, the time interval threshold is set to ± 60 min, and the nearest FY-4A AGRI LPW product within the time interval is searched for matching data. For ERA-5, the time threshold is set to ± 30 min.

4.2. Spatial Collocation

For radiosonde data, based on the FY-4A pixels as a center, the sounding stations were searched in a 20 km radius area. The sounding data of the matched station were compared with AGRI LPW products. Same as radiosonde data, the FY-4A pixels were also used as the center to search the Himawari-8 AHI and MODIS pixels in a 5 km radius area. All matched Himawari-8 AHI and MODIS pixels were compared with AGRI LPW products. The global model water vapor profile data (include ERA-5, NCEP and T639 data) used in this study were with different spatial resolution, 2.5° grid for NCEP, 0.25° grid for ERA-5 and 0.28125° grid for T639 data. FY-4A products were resampled to the same spatial grid as global model water vapor profile data separately to complete the spatial collocation.

5. Results

The QCS automatically collocates the AGRI LPW product with three types of evaluating data, including radiosonde data, model data and satellite data, and generates various evaluation results in near real time. Figures with statistical results are automatically generated from those evaluations and are continuously monitored to ensure the quality of the AGRI LPW products. This study shows the monthly evaluation results for the month of November 2019, and more comprehensive statistics for longer period from 23rd October 2019 to 15th November 2020. These are done for both full disc and the China region. All figures and statistic results in this paper were generated by QCS.

5.1. Evaluation with Radiosonde Data

Monthly mean bias distribution maps of TPWs and LPWL by radiosonde data for November 2019 were shown in Figure 1. From Figure 1a,c, positive bias was mainly located in low latitude area. From Figure 1b,d, the large bias stations were mainly located in southeast China area. That is reasonable because that is the region with more moisture than the rest part of China.

Figures 2 and 3 show scatter plots and histograms of TPW and LPWL between AGRI and radiosonde data. From these Figures, it can be seen that FY-4A TPW and LPWL products were with good consistency to radiosonde data, especially for TPW.

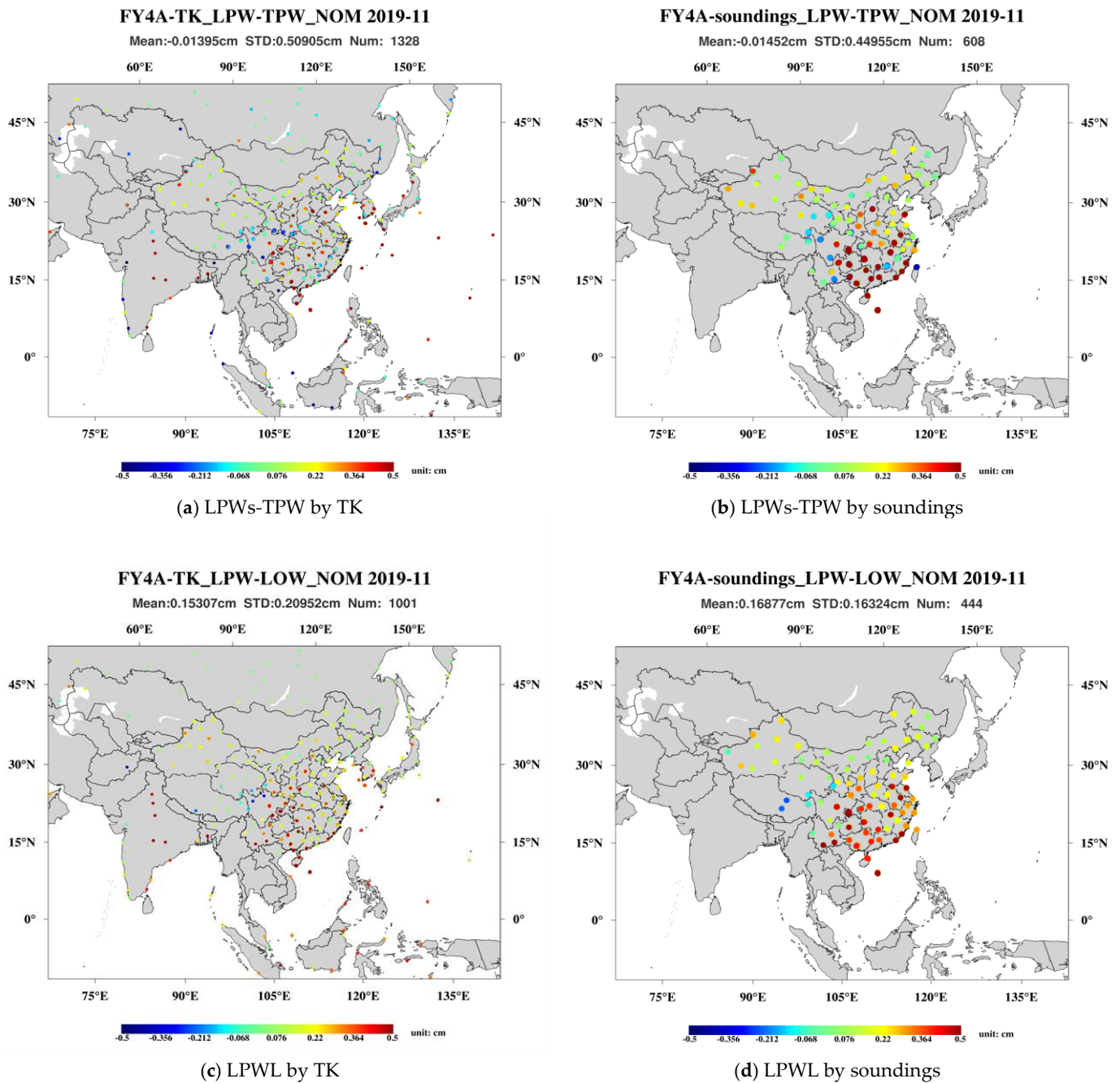


Figure 1. Monthly bias spatial distribution of TPW and LPWL between FY-4A and evaluating data from radiosonde data for November 2019, including (a,c) TK coverage is 70 °E to 140 °E and from 15 °S to 50 °N, (b,d) soundings, coverage is China area.

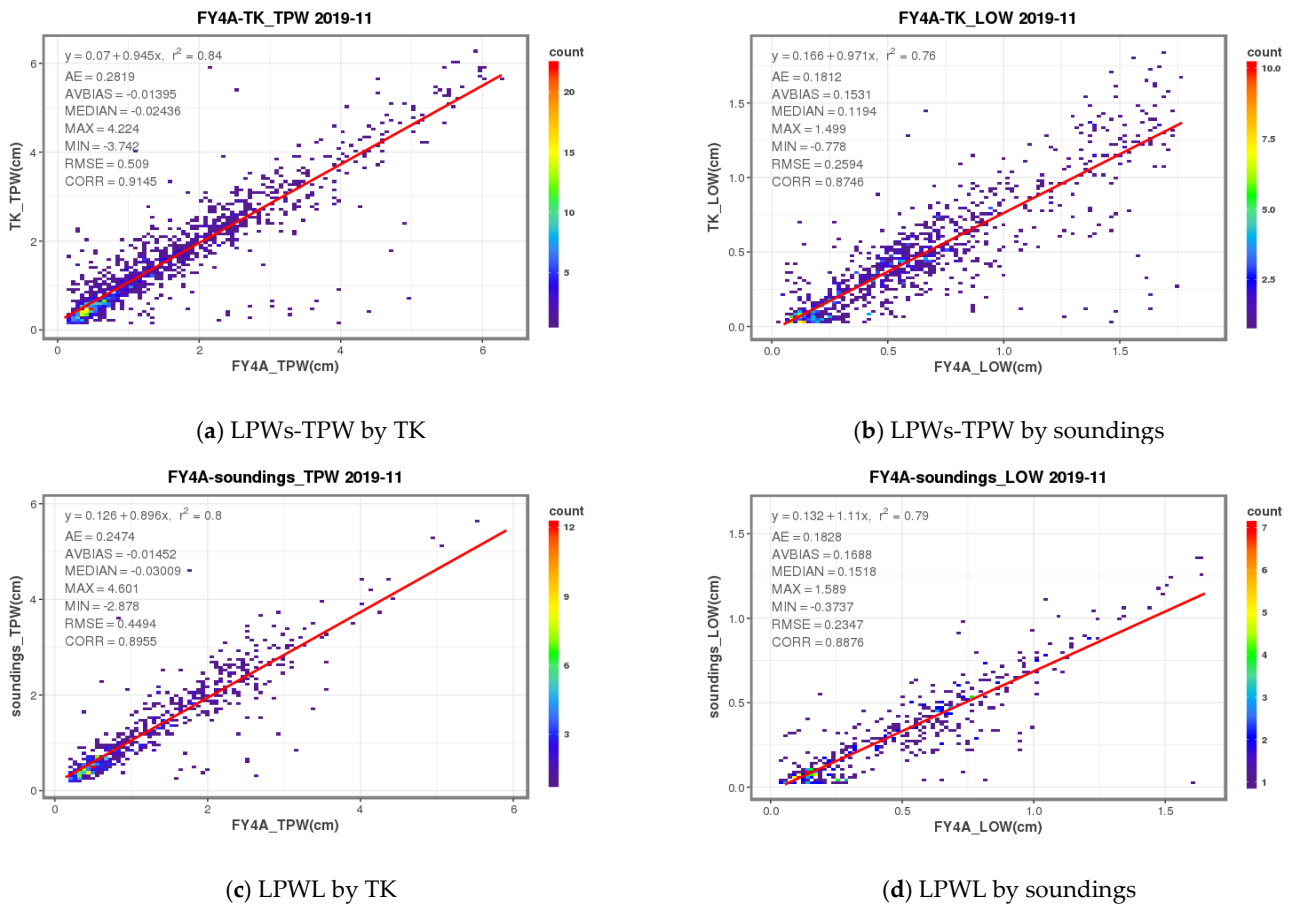
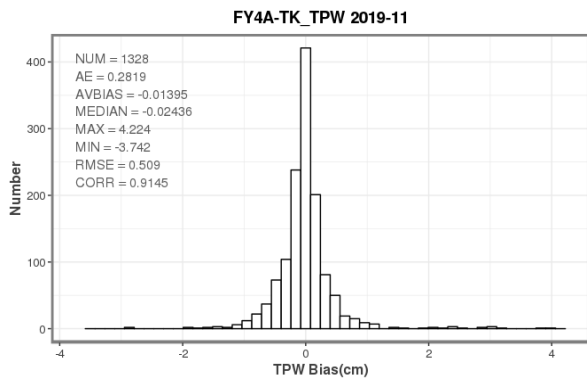


Figure 2. Scatter plot of TPW (left) and LPWL (right) between the FY-4A AGRI product (x-axis) and the RAOB (y-axis). Upper panels use the “TK” RAOB and lower panels use the “Soundings” RAOB. Data is from November 2019. (a) LPWs-TPW by TK (b) LPWs-TPW by soundings (c) LPWL by TK (d) LPWL by soundings.

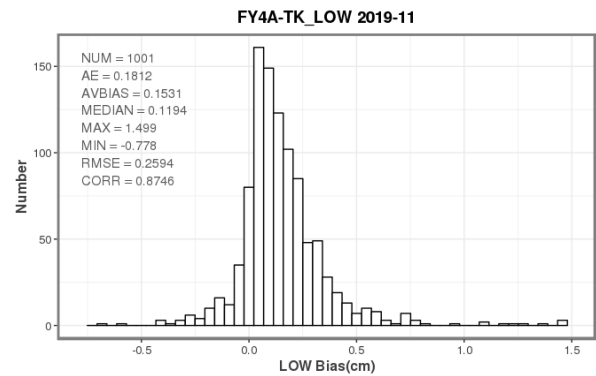
Monthly statistical analysis of differences between AGRI TPW/LPWL and radiosonde data were listed in Table 2. The time coverage of the data pairs was November 2019.

Table 2. FY-4A LPWs product evaluating errors statistics with radiosonde data as reference. Unit: cm.

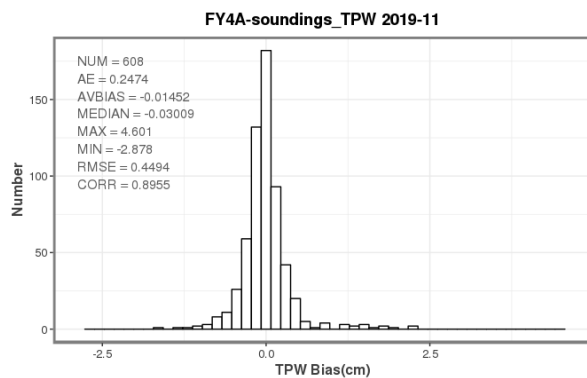
LPWs	Evaluating Data Source	Mean Bias	Absolute Bias	RMSE	Median Bias	Maximum Bias	Minimum Bias	Correlation Coefficient
TPW	TK	−0.0140	0.2819	0.5090	−0.0277	4.2240	−3.7420	0.9145
	soundings	−0.0145	0.2474	0.4494	−0.0301	4.6010	−2.8780	0.8955
LOW	TK	0.1531	0.1812	0.2594	0.1194	1.4990	−0.7780	0.8746
	soundings	0.1688	0.1828	0.2347	0.1518	1.5890	−0.3737	0.8876



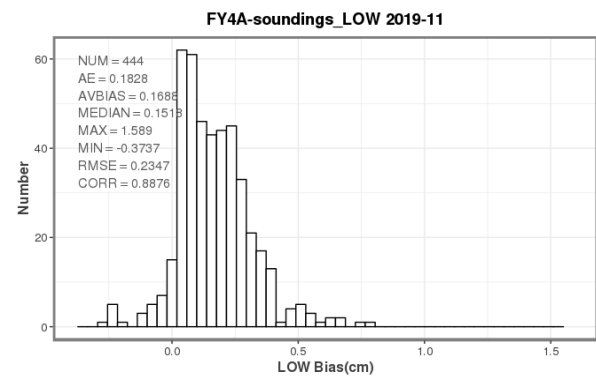
(a) LPWs-TPW by TK



(b) LPWs-TPW by soundings



(c) LPWL by TK



(d) LPWL by soundings

Figure 3. The histograms of the differences of TPW (left) and LPWL (right) between FY-4A AGRI and RAOB (former minus latter). Upper panels use “TK” RAOB, and lower panels use “Sounding” RAOB. Data is from November 2019. (a) LPWs-TPW by TK (b) LPWs-TPW by soundings (c) LPWL by TK (d) LPWL by soundings.

A good sounding product should have temporally stable biases. Figure 4 shows the 12-hourly time series of the TPW/LPWL bias and STD compared with different radiosonde dataset from 23rd October 2019 to 20th February 2020. The black lines in each subplot showed the mean bias and the grey area showed the STD of each data pair. From Figure 4 we can see that the bias was around 0 and STD was within ± 0.3 cm for whole comparing period except some outliers.

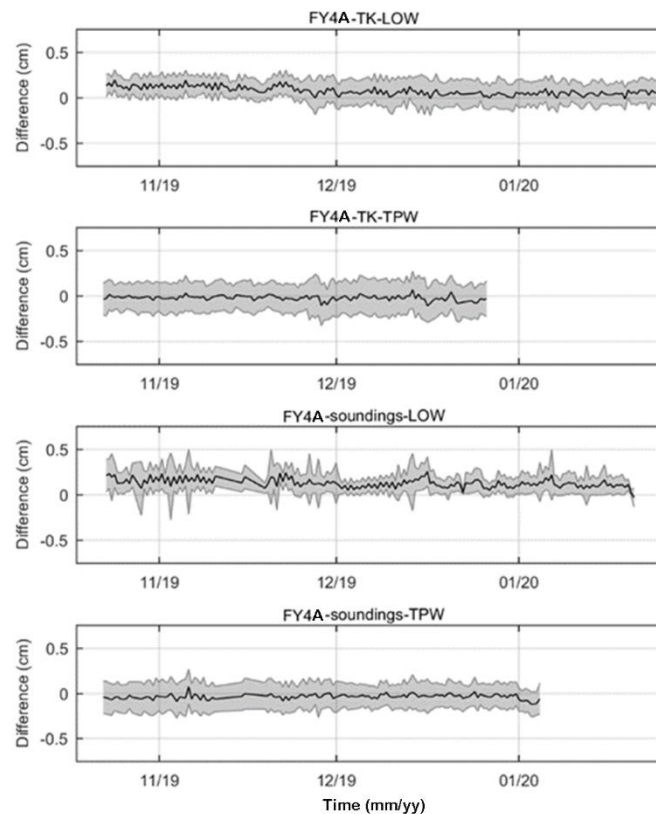
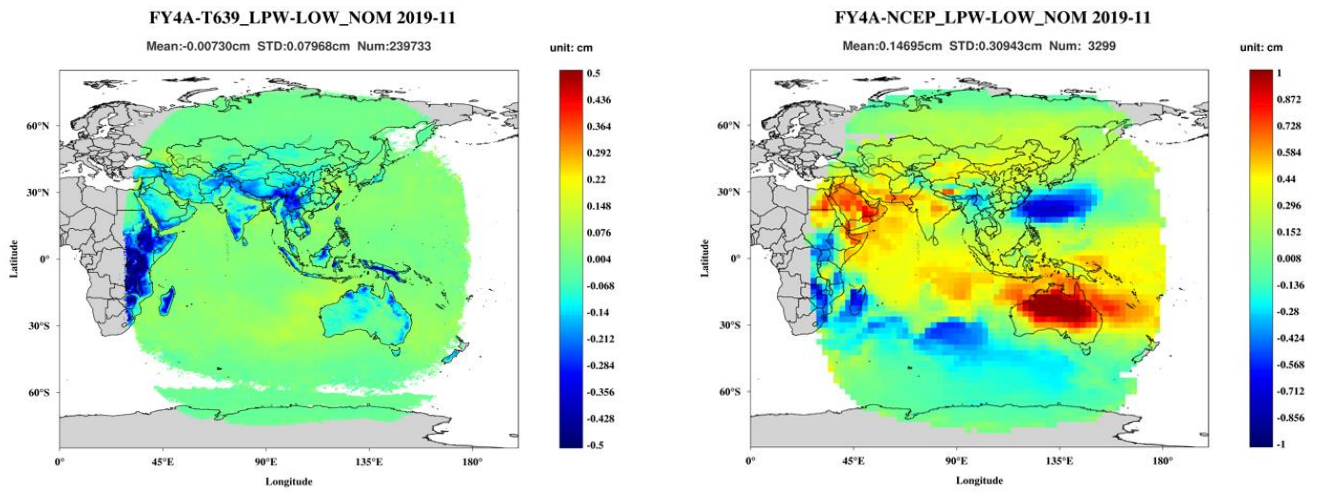


Figure 4. 12-hourly time series of TPW and LPWL bias (black lines) and STD (gray area) compared with RAOB.

5.2. Evaluation with Model Data

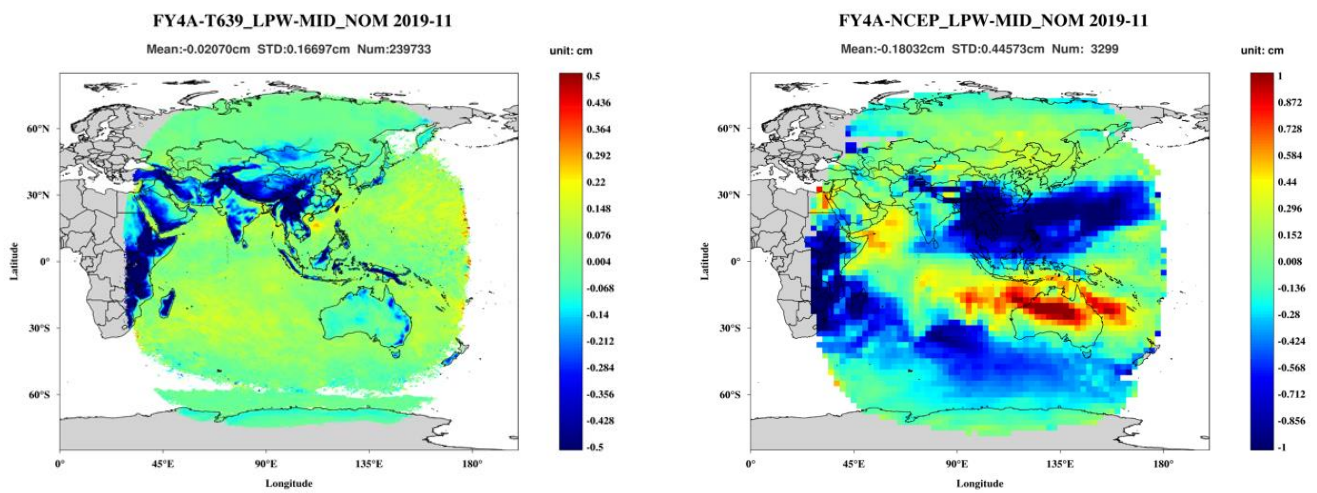
Same as comparisons with radiosonde data, the evaluation results with model data for November 2019 were also shown in geographic map, scatter plots, histograms and time series for 3 LPWs. From Figure 5a,c,e, the consistent significant negative bias can be seen in Tibet, India, Arabian, Africa when compared with T639. In Figure 5b two big bias areas with opposite values in symmetrical areas across equator around Southeast Asia, are identified. This phenomenon didn't appear in the bias distribution map with T639 products (Figure 5a). From Figure 5b,d,f, the consistent significant negative bias can be seen over Pacific Ocean off southeast Asia and the south Indian Ocean, and positive bias over Australia and nearby oceans when compared with NCEP.

Figures 6 and 7 show scatter plots and histograms of differences between AGRI and model data for LPWL/LPWM/LPWH. From these figures, FY-4A LPW products were with good consistency to model data. From Figure 7, for NCEP data low layer, there were bi-peak shape in histogram. That is because two big bias area with opposite values in symmetrical area across equator showed in Figure 5b. The monthly detailed evaluation statistics were listed in Table 3.



(a) LPWL by T639

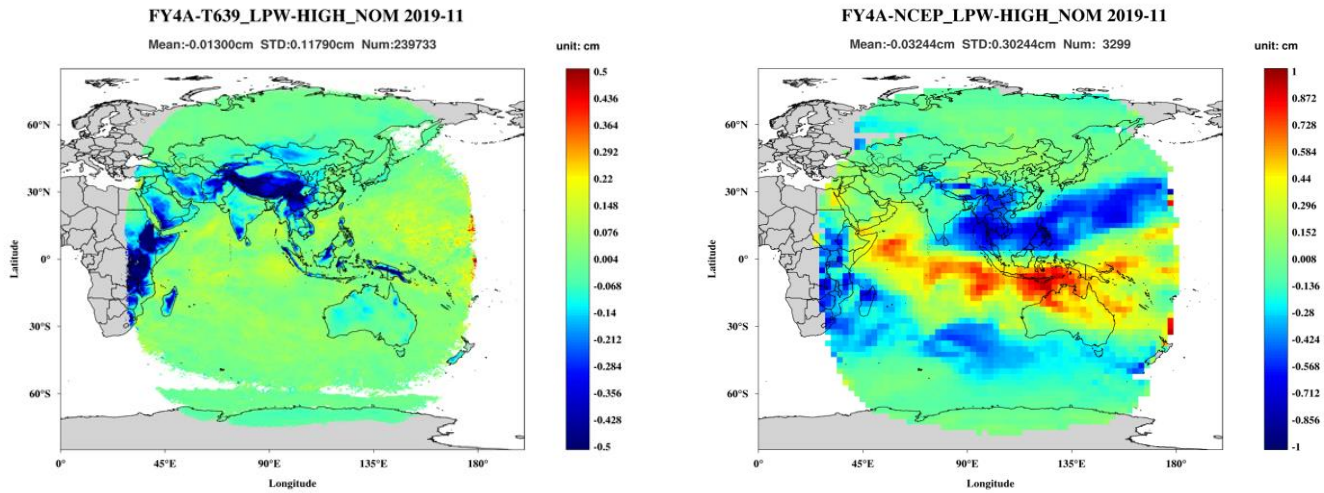
(b) LPWL by NCEP



(c) LPWM by T639

(d) LPWM by NCEP

Figure 5. Cont.



(e) LPWH by T639

(f) LPWH by NCEP

Figure 5. The bias geographic distribution of different LPWs (top: LPWL, middle: LPWM, bottom: LPWH) when compared with the different model data (left: CMA T639, and right: NCEP) for November of 2019. (a) LPWL by T639 (b) LPWL by NCEP (c) LPWM by T639 (d) LPWM by NCEP (e) LPWH by T639 (f) LPWH by NCEP.

Table 3. FY-4A LPWs product evaluating errors statistics by model data. Unit: cm.

LPWs	Evaluating Data Source	Mean Bias	Absolute Bias	RMSE	Median Bias	Maximum Bias	Minimum Bias	Correlation Coefficient
LOW	NCEP	0.1470	0.2725	0.3425	0.1610	1.3220	-0.7801	0.8452
	T639	-0.0073	0.0470	0.0800	-0.0076	0.3518	-0.6536	0.9905
MID	NCEP	-0.1803	0.3521	0.4808	-0.1287	1.2840	-2.0070	0.8081
	T639	-0.0207	0.0909	0.1682	-0.0095	0.8221	-1.5060	0.9781
HIGH	NCEP	-0.0324	0.2293	0.3041	-0.0493	0.9520	-0.8207	0.7495
	T639	-0.0130	0.0639	0.1186	-0.0041	1.2210	-1.2650	0.9651

Figure 8 shows 6-hourly time series of the 3 LPWs bias and STD with different model data from 23 October 2019 to 15 November 2020. From Figure 8, we can see that AGRI LPW products were with very good consistency to T639, NCEP and ERA5, not only in bias but also in STD. For T639 data, the biases are around 0 cm and the STD were less than 0.2 cm, except for LPWH around 0.4 cm; for NCEP data there were also with a bias around 0 cm, but the STD were less than 0.3 cm in all three layers. For ERA5 data, only MID layer was compared and also with good consistency.

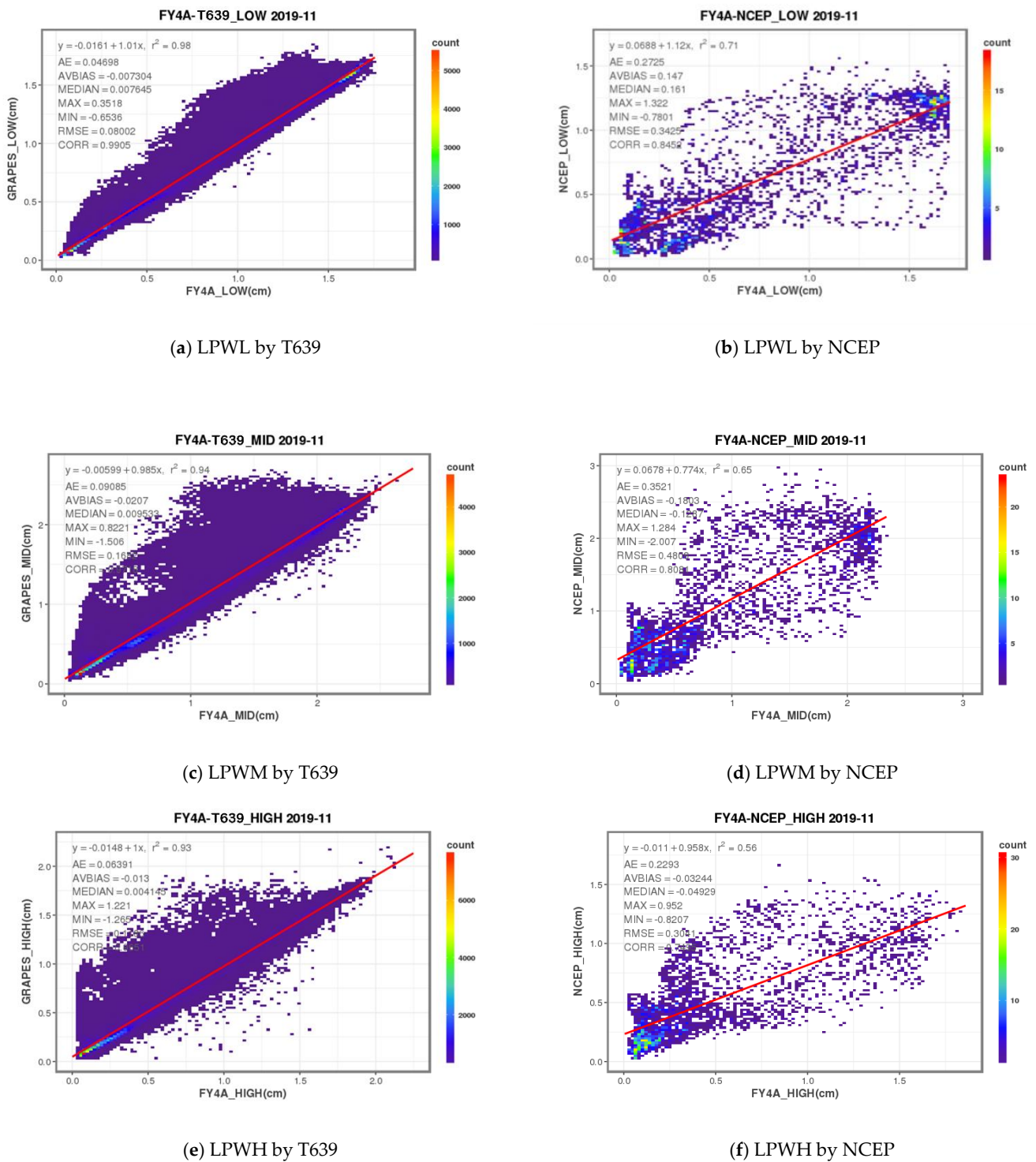
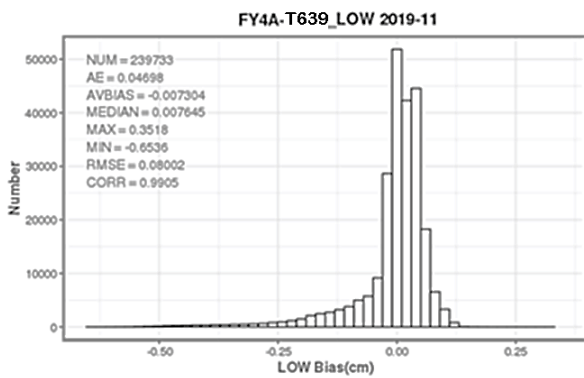
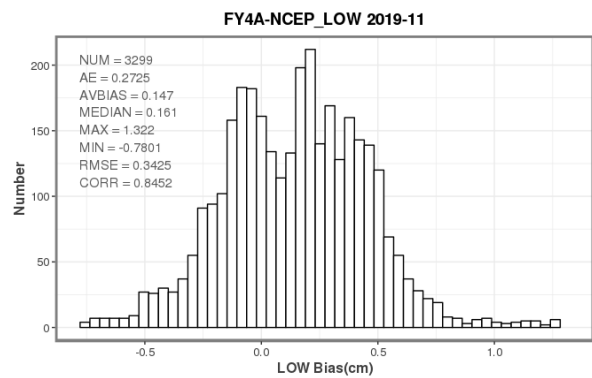


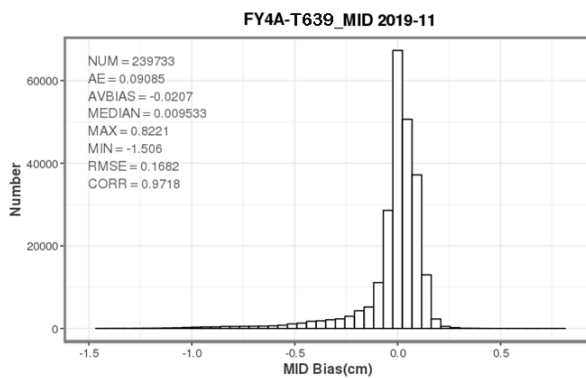
Figure 6. Scatter plot of LPWL, LPWM, and LPWH between FY-4A AGRI retrievals and different model datasets (left: CMA T639, right: NCEP) for November 2019. (a) LPWL by T639 (b) LPWL by NCEP (c) LPWM by T639 (d) LPWM by NCEP (e) LPWH by T639 (f) LPWH by NCEP.



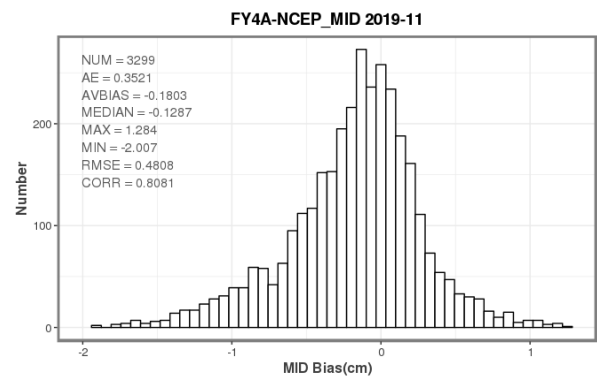
(a) LPWL by T639



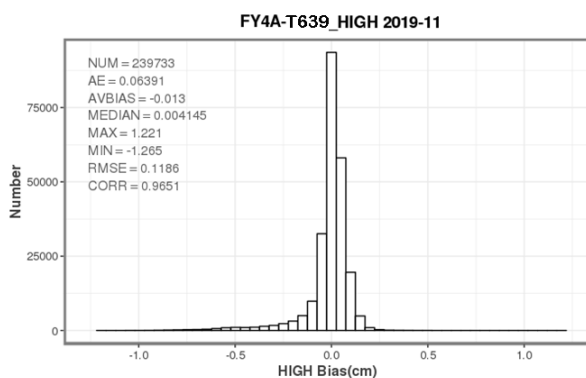
(b) LPWL by NCEP



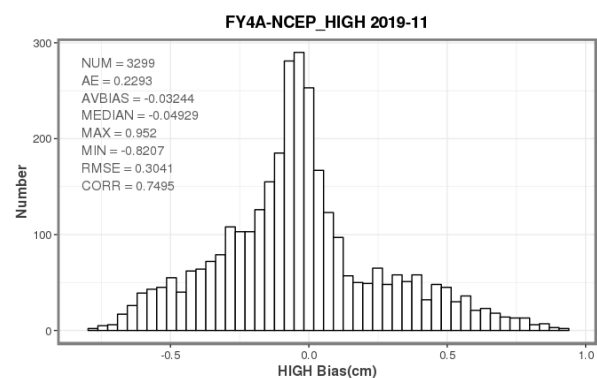
(c) LPWM by T639



(d) LPWM by NCEP



(e) LPWH by T639



(f) LPWH by NCEP

Figure 7. The histograms of the differences of LPWL/LPWM/LPWH between FY-4A AGRI and different model datasets (left: CMA T639, right: NCEP and former minus latter) for November 2019. (a) LPWL by T639 (b) LPWL by NCEP (c) LPWM by T639 (d) LPWM by NCEP (e) LPWH by T639 (f) LPWH by NCEP.

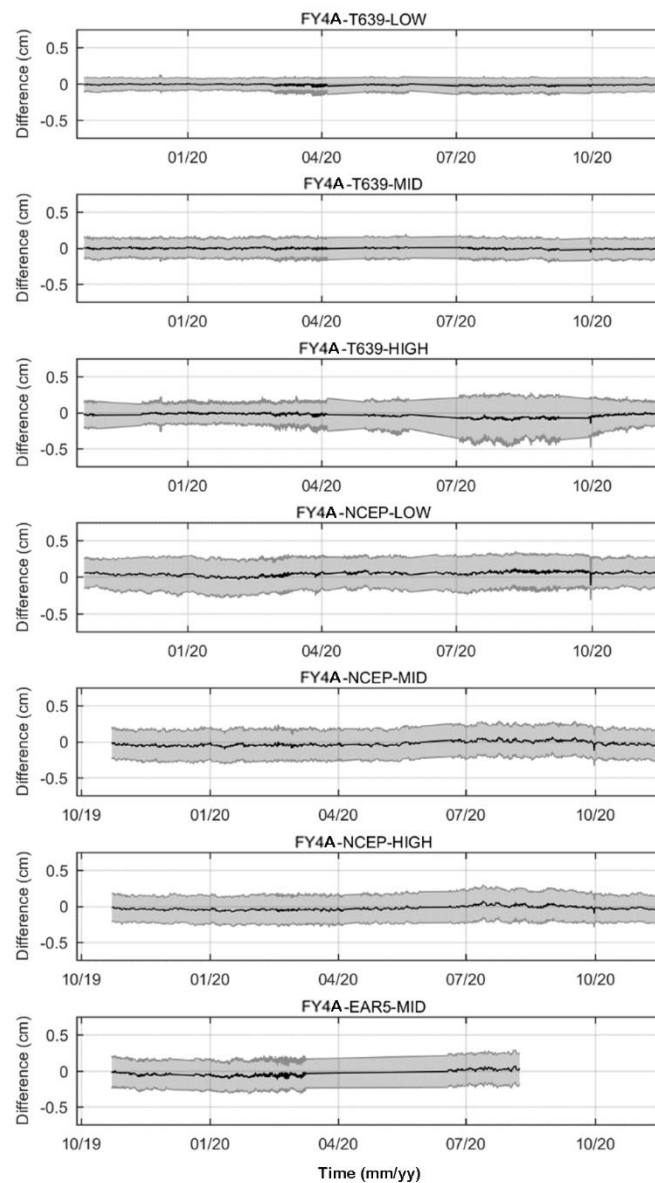


Figure 8. 6-hourly time series of LPWL/LPWM/LPWH bias (black line) and STD (gray area) with different model data from 23 October 2019 to 15 November 2020.

5.3. Inter-Comparison with Other Satellite Retrieval Products

The AGRI TPW and LPW products were also evaluated by inter-comparing with other satellite retrieval products from AHI and MOD05. The results for November 2019 were shown in geographic maps, scatter plots, histograms, and time series. Because MOD05 only has TPW product. The comparison between AGRI and MOD05 was only carried out with TPW. The comparison with AHI is also focused on TPW. The monthly accumulated bias distribution map of TPW was shown in Figure 9. From Figure 9a, we can see that there is an area with large positive bias around equator and ocean area. This is likely caused by MOD05 because AGRI TPW shows no such pattern when compared with different model data. And the positive bias appears to be related to cloud contamination. To verify that, Figure 10 shows the mean brightness temperature of FY-4A AGRI 10.8 μm every 6 h from 1 to 30 November 2020, totally 121 time observing data. The region with positive bias in Figure 9a is clearly an indication of more likelihood of being affected by clouds with colder

BTs than surrounding area. The MOD05 algorithm, as a result, underestimates TPW of the region, leading to positive bias in Figure 9a.

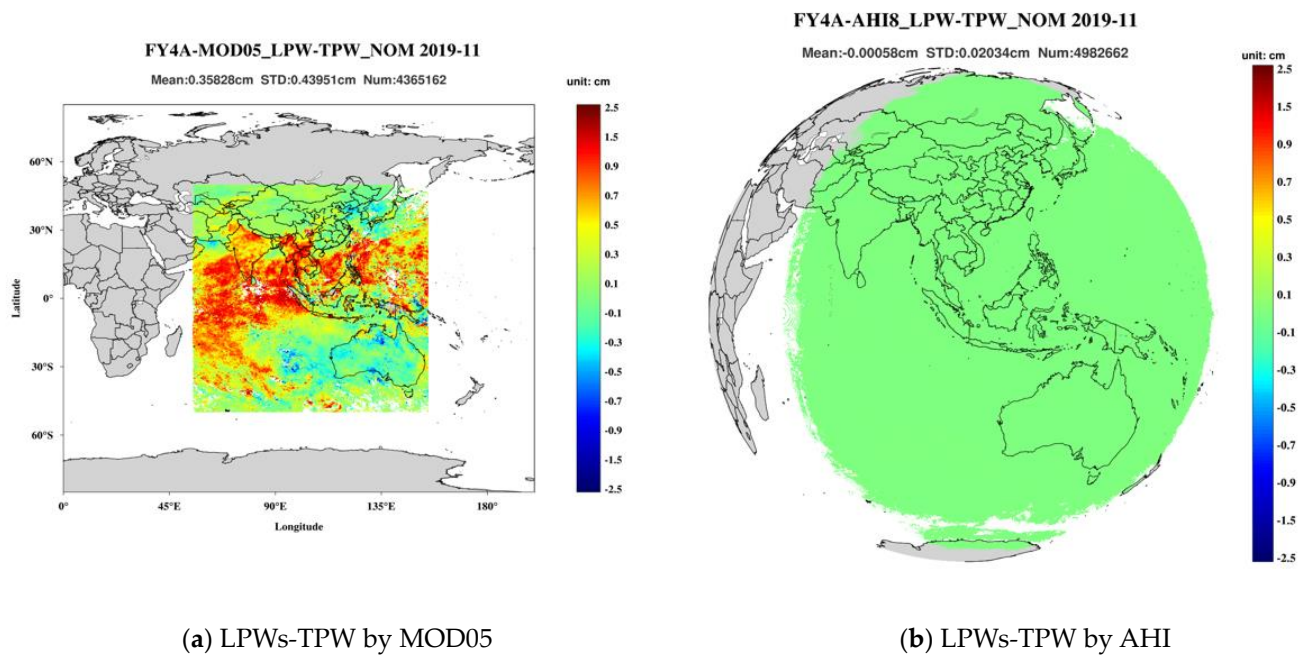


Figure 9. Bias distribution map of LPWs TPW with satellite data (a) MOD05, (b) AHI for November 2019.

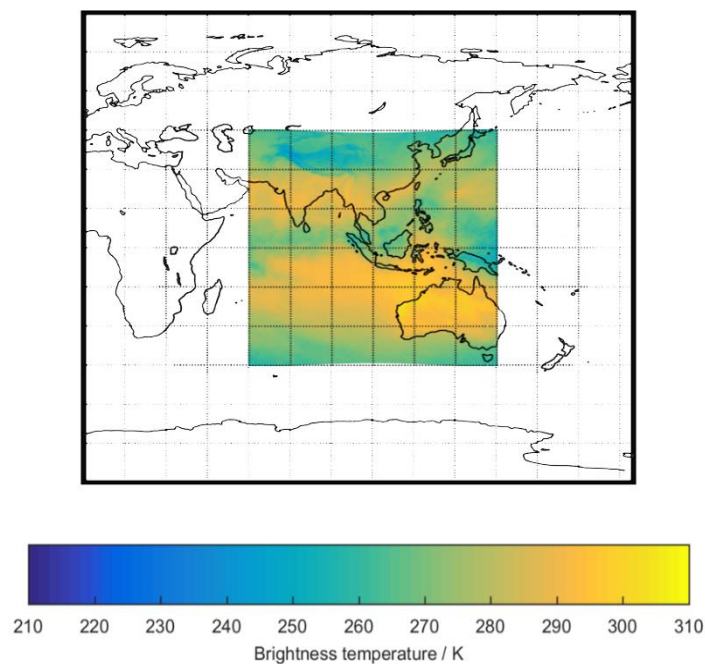


Figure 10. FY-4A AGRI ch12's monthly mean brightness temperature of November 2019.

Figures 11 and 12 shows scatter plots of TPW and histograms of TPW differences between FY-4A AGRI and AHI/MOD05. Each figure showed sample number, mean bias, maximum bias, minimum bias, root mean square value and so on. More detailed numbers were listed in Table 4. From these Figures and Tables, it can be seen that FY-4A TPW product was with good consistency to different evaluation sources. For AHI and MOD05, they are two types of satellite-based data, the monthly accumulated samples were very large numbers and with smaller bias.

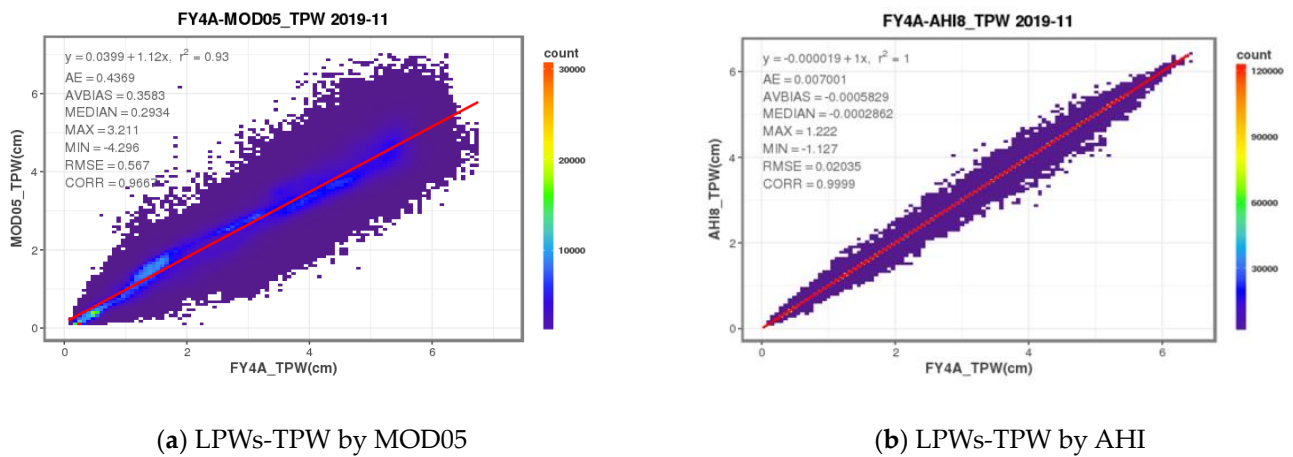


Figure 11. Scatter plot of TPW between FY-4A AGRI and satellite data (a) MOD05, (b) AHI for November 2019.

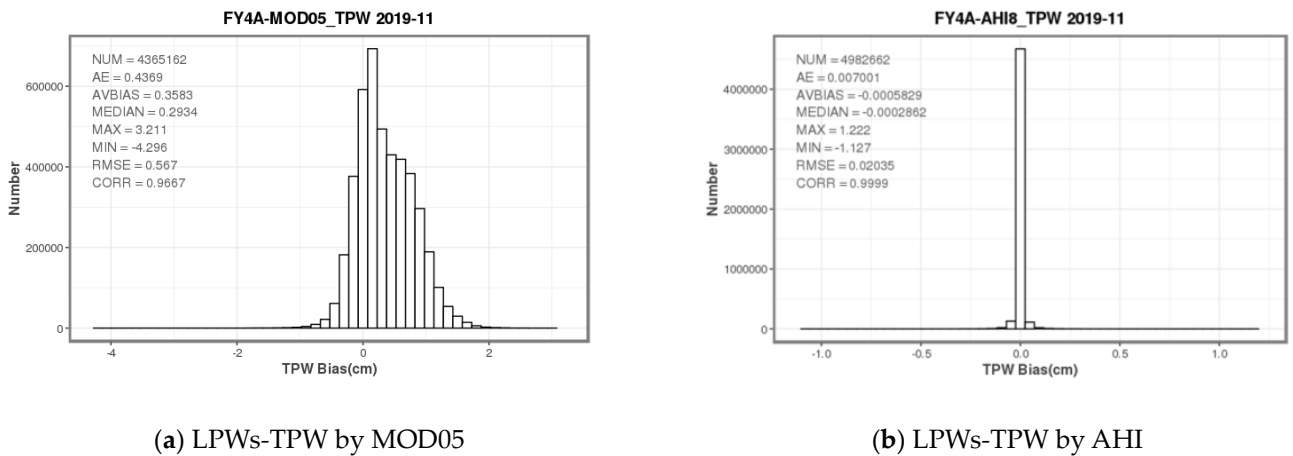


Figure 12. The histograms of the differences of TPW between FY-4A AGRI and satellite data (a) MOD05, (b) AHI and former minus latter for November 2019.

Table 4. FY-4A LPWs-TPW product evaluating errors statistics by satellite retrievals. Unit: cm.

Evaluating Data Source	Mean Deviation	Absolute Deviation	RMSE	Median Deviation	Maximum Deviation	Minimum Deviation	Correlation Coefficient
MOD05	0.3583	0.4369	0.5670	0.2934	3.2110	-4.2960	0.9667
AHI	-0.0006	0.0070	0.0204	-0.0003	1.2220	-1.1270	0.9999

Figure 13 shows the hourly time series of the TPW bias from comparisons with the reference dataset from 27 October to 3 December 2019 for MOD05 and 22 October to 7 December 2019 for AHI. The black lines in each subplot showed the mean bias and the grey area showed the STD of each data pair. From Figure 13 we can see that the bias and STD between AGRI and AHI were almost 0 for all data pairs. The AGRI and AHI agree with each other so well mainly because they use the same physical retrieval algorithm and the same NWP background. So, the differences between them should be mainly caused by the differences in the two sensors, which appears to be small. For, AGRI and MOD05, the bias and STD change rapidly in different dates, the mean bias was around 0.2 cm and the STD was within 0.3 cm, respectively.

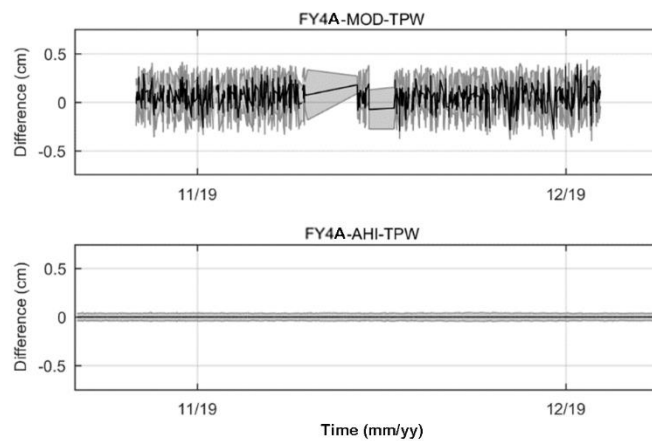


Figure 13. The hourly time series of TPW differences between FY-4A AGRI and satellite data, which MOD05 from 27 October to 3 December 2019 (**top**) and AHI from 22 October to 7 December 2019 (**bottom**). The black lines in each subplot showed the mean bias and the grey area showed the STD.

6. Conclusions and Discussion

The FY-4A AGRI retrieved sounding products have been comprehensively evaluated using various reference sources automatically based on QCS of FY-4A, including in-situ, model data, and other satellite measurements. Evaluation report can be generated automatically by each month.

The FY-4A AGRI LPWs product is integrated from the moisture sounding profile for three layers in sigma coordinate: surface–0.9, 0.9–0.7, 0.7–0.3 and total precipitable water vapor. With the higher temporal resolution from AGRI, the LPWs products are now available for 40 full disk observations and 165 China area observations daily. It provides forecasters moisture information in TPW, lower, middle, and upper troposphere. From this study, the quality of AGRI LPWs products is favorable and stable. These evaluation results show that the AGRI LPWs products have reasonable quality, and are ready for operational use. And the QCS is a useful tool to monitor, evaluate, and validate the AGRI LPW products. The AGRI LPWs products are available in NetCDF via National Satellite Meteorological Center’s (NSMC) FENGYUN Satellite Data Center [55].

Author Contributions: Conceptualization, Y.Z.; methodology, Y.Z., Z.L. and J.Z.; software, D.W. and H.Z.; formal analysis, J.L. and Z.L.; data curation, Y.Z. and J.Z.; writing—original draft preparation, Y.Z.; writing—review and editing, Y.Z., J.L., Z.L. and J.Z. All authors have read and agreed to the published version of the manuscript.

Funding: This research was funded by Technical Pre-research Project of Civil Aerospace, grant number D040401 and Shanghai Aerospace Science and Technology Innovation Fund Project, grant number SAST2019-044.

Institutional Review Board Statement: Not applicable.

Informed Consent Statement: Not applicable.

Data Availability Statement: The T639 data were obtained via <http://data.cma.cn/data/detail/dataCode/F.0003.0001.html>, (accessed on 29 January 2022). ERA-5 products used are available from ECMWF (<https://www.ecmwf.int/en/forecasts/dataset/ecmwf-reanalysis-v5>, accessed on 29 January 2022). NCEP Reanalysis data provided by the NOAA/OAR/ESRL PSL, Boulder, Colorado, USA, from their Web site at <https://psl.noaa.gov/data/gridded/reanalysis/>, accessed on 29 January 2022. Himawari-8 L1 Gridded data is provided by the Japan Meteorological Agency (https://www.data.jma.go.jp/mscweb/en/himawari89/cloud_service/cloud_service.html, accessed on 29 January 2022). Radiosonde data are available from the University of Wyoming (<http://weather.uwyo.edu/upperair/sounding.html>, accessed on 29 January 2022) and the China Meteorological Administration (<http://data.cma.cn/data/cdcindex/cid/565b6087618affa1.html>, accessed on 29 January 2022).

Acknowledgments: The authors would like to acknowledge, with thanks, the contribution from the colleagues who worked on the FY-4A engineering program in the National Satellite Meteorological Center of China Meteorological Administration. The authors also thank the anonymous reviewers for their valuable comments and suggestions to improve the quality of this article.

Conflicts of Interest: The authors declare no conflict of interest.

References

1. Jun, Y.; Zhang, Z.; Wei, C.; Lu, F.; Guo, Q. Introducing the new generation of Chinese geostationary weather satellites, FENGYUN-4. *Bull. Am. Meteor. Soc.* **2017**, *98*, 1637–1658.
2. National Satellite Meteorological Center Home Page. Available online: <http://www.nsmc.org.cn/nsmc/en/theme/FY4B.html> (accessed on 29 January 2022).
3. Min, M.; Wu, C.; Li, C.; Liu, H.; Xu, N.; Wu, X.; Chen, L.; Wang, F.; Sun, F.; Qin, D.; et al. Developing the science product algorithm testbed for Chinese next-generation geostationary meteorological satellites: Fengyun-4 series. *J. Meteorol. Res.* **2017**, *31*, 708–719. [[CrossRef](#)]
4. Schmit, T.J.; Gunshor, M.M.; Menzel, W.P.; Gurka, J.; Li, J.; Bachmeier, S. Introducing the next-generation Advanced Baseline Imager (ABI) on GOES-R. *Bull. Am. Meteor. Soc.* **2005**, *86*, 1079–1096. [[CrossRef](#)]
5. Schmit, T.J.; Griffith, P.; Gunshor, M.M.; Daniels, J.M.; Goodman, S.J.; Lehair, W.J. A closer look at the ABI on the GOES-R series. *Bull. Am. Meteor. Soc.* **2017**, *98*, 681–698. [[CrossRef](#)]
6. EUMETSAT Home Page. Available online: <https://www.eumetsat.int/mtg-flexible-combined-imager> (accessed on 29 January 2022).
7. Solomon, S.; Rosenlof, K.H.; Portmann, R.W.; Daniel, J.S.; Davis, S.M.; Sanford, T.J.; Plattner, G.K. Contributions of stratospheric water vapor to decadal changes in the rate of global warming. *Science* **2010**, *327*, 1219–1223. [[CrossRef](#)]
8. Wagner, T.; Beirle, S.; Grzegorski, M.; Platt, U. Global trends (1996–2003) of total column precipitable water observed by global ozone monitoring experiment (GOME) on ERS-2 and their relation to near-surface temperature. *J. Geophys. Res. Atmos.* **2006**, *111*, 2193–2214. [[CrossRef](#)]
9. Held, I.M.; Soden, B.J. Water vapor feedback and global warming. *Annu. Rev. Energy Environ.* **2000**, *25*, 441–475. [[CrossRef](#)]
10. Trenberth, K.E.; Fasullo, J.; Smith, L. Trends and variability in column-integrated atmospheric water vapor. *Clim. Dyn.* **2005**, *24*, 741–758. [[CrossRef](#)]
11. Durre, I.; Vose, R.S.; Wuertz, D.B. Overview of the integrated global radiosonde archive. *J. Clim.* **2006**, *19*, 53–68. [[CrossRef](#)]
12. Alexandrov, M.D.; Schmid, B.; Turner, D.D.; Cairns, B.; Oinas, V.; Lacis, A.A.; Gutman, S.I.; Westwater, E.R.; Smirnov, A.; Eilers, J. Columnar water vapor retrievals from multifilter rotating shadow band radiometer data. *J. Geophys. Res. Atmos.* **2009**, *114*, D02306. [[CrossRef](#)]
13. Cadeddu, M.P.; Liljegren, J.C.; Turner, D.D. The atmospheric radiation measurement (ARM) program network of microwave radiometers: Instrumentation, data, and retrievals. *Atmos. Meas. Tech.* **2013**, *6*, 2359–2372. [[CrossRef](#)]
14. Xu, G.R.; Ware, R.; Zhang, W.G.; Feng, G.L.; Liao, K.W.; Liu, Y.B. Effect of offzenith observations on reducing the impact of precipitation on ground-based microwave radiometer measurement accuracy. *Atmos. Res.* **2014**, *140*, 85–94. [[CrossRef](#)]
15. Sánchez, J.L.; Posada, R.; García-Ortega, E.; López, L.; Marcos, J.L. A method to improve the accuracy of continuous measuring of vertical profiles of temperature and water vapor density by means of a ground-based microwave radiometer. *Atmos. Res.* **2013**, *122*, 43–54. [[CrossRef](#)]
16. Wang, M.; Fang, X.; Hu, S.X.; Hu, H.L.; Li, T.; Dou, X.K. Variation characteristics of water vapor distribution during 2000–2008 over Hefei (31.9° N, 117.2° E) observed by L625 lidar. *Atmos. Res.* **2015**, *164*, 1–8. [[CrossRef](#)]
17. Whiteman, D.N.; Cadirola, M.; Venable, D.; Calhoun, M.; Miloshevich, L.; Vermeesch, K.; Twigg, L.; Dirisu, A.; Dirisu, D.; Hall, E.; et al. Correction technique for Raman water vapor lidar signal-dependent bias and suitability for water vapor trend monitoring in the upper troposphere. *Atmos. Meas. Tech.* **2012**, *5*, 2893–2916. [[CrossRef](#)]
18. Champollion, C.; Masson, F.; Bouin, M.N.; Walpersdorf, A.; Doerflinger, E.; Bock, O.; Van Baelen, J. GPS water vapour tomography: Preliminary results from the ESCOMPTE field experiment. *Atmos. Res.* **2005**, *74*, 253–274. [[CrossRef](#)]
19. Elgered, G.; Johansson, J.M.; Rönnäng, B.O.; Davis, J.L. Measuring regional atmospheric water vapor using the Swedish permanent GPS network. *Geophys. Res. Lett.* **1997**, *24*, 2663–2666. [[CrossRef](#)]
20. Wang, J.; Zhang, L.; Dai, A.; Van Hove, T.; Van Baelen, J. A near-global, 2-hourly data set of atmospheric precipitable water from ground-based GPS measurements. *J. Geophys. Res. Atmos.* **2007**, *112*, 236–242. [[CrossRef](#)]
21. Gao, B.C.; Kaufman, Y.J. Water vapor retrievals using Moderate Resolution Imaging Spectroradiometer (MODIS) near-infrared channels. *J. Geophys. Res. Atmos.* **2003**, *108*, 4389. [[CrossRef](#)]
22. Nelson, R.R.; Crisp, D.; Ott, L.E.; O'Dell, C.W. High-accuracy measurements of total column water vapor from the orbiting carbon observatory-2. *Geophys. Res. Lett.* **2016**, *43*, 12261–12269. [[CrossRef](#)]
23. Niell, A.E.; Coster, A.J.; Solheim, F.S.; Mendes, V.B.; Toor, P.C.; Langley, R.B.; Upham, C.A. Comparison of measurements of atmospheric wet delay by radiosonde, water vapor radiometer, GPS, and VLBI. *J. Atmos. Ocean. Technol.* **2001**, *18*, 830–850. [[CrossRef](#)]

24. Adeyemi, B.; Joerg, S. Analysis of water vapor over Nigeria using radiosonde and satellite data. *J. Appl. Meteorol. Climatol.* **2012**, *51*, 1855–1866. [[CrossRef](#)]
25. Seemann, S.W.; Li, J.; Menzel, W.P.; Gumley, L.E. Operational retrieval of atmospheric temperature, moisture, and ozone from MODIS infrared radiances. *J. Appl. Meteorol.* **2003**, *42*, 1072–1091. [[CrossRef](#)]
26. King, M.D.; Kaufman, Y.J.; Menzel, W.P.; Tanre, D. Remote sensing of cloud, aerosol, and water vapor properties from the moderate resolution imaging spectrometer (MODIS). *IEEE Trans. Geosci. Remote Sens.* **1992**, *30*, 2–27. [[CrossRef](#)]
27. Kaufman, Y.J.; Gao, B.C. Remote sensing of water vapor in the near IR from EOS/MODIS. *IEEE Trans. Geosci. Remote Sens.* **1992**, *30*, 871–884. [[CrossRef](#)]
28. Gao, B.C.; Chan, P.K.; Li, R.R. A global water vapor data set obtained by merging the SSMI and MODIS data. *Geophys. Res. Lett.* **2004**, *31*, L18103. [[CrossRef](#)]
29. McAtee, B.K.; Maier, S.W. A comparison of algorithms for near-real time water vapour retrieval from MODIS. *Int. J. Remote Sens.* **2006**, *27*, 5145–5163. [[CrossRef](#)]
30. Liu, J.; Liang, H.; Sun, Z.; Zhou, X. Validation of the moderate-resolution imaging spectroradiometer precipitable water vapor product using measurements from GPS on the Tibetan Plateau. *J. Geophys. Res. Atmos.* **2006**, *111*, 1–5. [[CrossRef](#)]
31. Liu, Z.; Wong, M.S.; Nichol, J.; Chan, P.W. A multi-sensor study of water vapour from radiosonde, MODIS and AERONET: A case study of Hong Kong. *Int. J. Climatol.* **2013**, *33*, 109–120. [[CrossRef](#)]
32. Liu, H.; Tang, S.; Zhang, S.; Hu, J. Evaluation of MODIS water vapour products over China using radiosonde data. *Int. J. Remote Sens.* **2015**, *36*, 680–690. [[CrossRef](#)]
33. Prasad, A.K.; Singh, R.P. Validation of MODIS Terra, AIRS, NCEP/DOE AMIP-II reanalysis-2, and AERONET sun photometer derived integrated precipitable water vapor using ground-based GPS receivers over India. *J. Geophys. Res. Atmos.* **2009**, *114*, 1–20. [[CrossRef](#)]
34. Wang, Y.; Yang, K.; Pan, Z.Y.; Qin, J.; Chen, D.L.; Lin, C.G.; Chen, Y.Y.; La, Z.; Tang, W.J.; Han, M.L.; et al. Evaluation of precipitable water vapor from four satellite products and four reanalysis datasets against GPS measurements on the Southern Tibetan Plateau. *J. Clim.* **2017**, *30*, 5699–5713. [[CrossRef](#)]
35. Menzel, W.P.; Schmit, T.J.; Zhang, P.; Li, J. Satellite-based atmospheric infrared sounder development and applications. *Bull. Am. Meteorol. Soc.* **2018**, *99*, 583–603. [[CrossRef](#)]
36. Ningombam, S.S.; Song, H.J.; Mugil, S.K.; Dumka, U.C.; Larson, E.J.L.; Kumar, B.; Sagar, R. Evaluation of fractional clear sky over potential astronomical sites. *Mon. Not. R. Astron. Soc.* **2021**, *507*, 3745–3760. [[CrossRef](#)]
37. Di, D.; Li, J.; Li, Z.; Li, J.; Schmit, T.J.; Menzel, W.P. Can current hyperspectral infrared sounders capture the small scale atmospheric water vapor spatial variations? *Geophys. Res. Lett.* **2021**, *48*, e2021GL095825. [[CrossRef](#)]
38. Menzel, W.P.; Purdom, J.F. Introducing GOES-I: The First of a New Generation of Geostationary Operational Environmental Satellites. *Bull. Am. Meteorol. Soc.* **1994**, *75*, 757–782. [[CrossRef](#)]
39. Menzel, W.P.; Holt, F.C.; Schmit, T.J.; Aune, R.M.; Schreiner, A.J.; Wade, G.S.; Gray, D.G. Application of GOES-8/9 Soundings to Weather Forecasting and Nowcasting. *Bull. Am. Meteorol. Soc.* **1998**, *79*, 2059–2078. [[CrossRef](#)]
40. Schmit, T.J.; Li, J.; Lee, S.J.; Li, Z.; Dworak, R.; Lee, Y.K.; Bowlan, M.; Gerth, J.; Martin, G.D.; Straka, W.; et al. Legacy atmospheric profiles and derived products from GOES-16: Validation and applications. *Earth Space Sci.* **2019**, *6*, 1730–1748. [[CrossRef](#)]
41. Zhang, Y.; Li, Z.L.; Li, J. A preliminary layer perceptible water vapor retrieval algorithm for FengYun-4 advanced geosynchronous radiation imager. In Proceedings of the IGARSS 2019—2019 IEEE International Geoscience and Remote Sensing Symposium, Yokohama, Japan, 28 July–2 August 2019; IEEE: Piscataway, NJ, USA, 2019; pp. 7564–7566.
42. Li, Z.; Li, J.; Menzel, W.P.; Schmit, T.J.; Nelson, J.P., III; Daniels, J.; Ackerman, S.A. GOES sounding improvement and applications to severe storm nowcasting. *Geophys. Res. Lett.* **2008**, *35*, L03806. [[CrossRef](#)]
43. Li, J.; Wolf, W.W.; Menzel, W.P.; Zhang, W.; Huang, H.-L.; Achtor, T.H. Global soundings of the atmosphere from ATOVS measurements: The algorithm and validation. *J. Appl. Meteorol.* **2000**, *39*, 1248–1268. [[CrossRef](#)]
44. You, Y.; Zhao, T.; Xie, Y.; Zheng, Y.; Zhu, J.; Xia, J.; Cao, L.; Wang, C.; Che, H.; Liao, Y.; et al. Variation of the aerosol optical properties and validation of MODIS AOD products over the eastern edge of the Tibetan Plateau based on ground-based remote sensing in 2017. *Atmos. Env.* **2020**, *223*, 117257. [[CrossRef](#)]
45. Jin, X.; Li, J.; Schmit, T.J.; Li, J.; Goldberg, M.D.; Gurka, J.J. Retrieving clear-sky atmospheric parameters from SEVIRI and ABI infrared radiances. *J. Geophys. Res.* **2008**, *113*, 1–19. [[CrossRef](#)]
46. Seemann, S.W.; Borbas, E.E.; Knuteson, R.O.; Stephenson, G.R.; Huang, H.-L. Development of a global infrared land surface emissivity database for application to clear sky sounding retrievals from multispectral satellite radiance measurements. *J. Appl. Meteorol. Climatol.* **2008**, *47*, 108–123. [[CrossRef](#)]
47. NOAA Center for Satellite Applications and Research Home Page. Available online: https://www.star.nesdis.noaa.gov/goesr/documents/ATBDs/Baseline/ATBD_GOES-R_Sounding_LAP_v3.0_July2012.pdf (accessed on 29 January 2022).
48. Lee, Y.K.; Li, Z.; Li, J.; Schmit, T.J. Evaluation of the GOES-R ABI LAP Retrieval Algorithm Using the GOES-13 Sounder. *J. Atmos. Ocean. Technol.* **2014**, *31*, 3–19. [[CrossRef](#)]
49. Lee, Y.K.; Li, J.; Li, Z.; Schmit, T. Atmospheric temporal variations in the pre-landfall environment of Typhoon Nangka (2015) observed by the Himawari-8 AHI. *Asia-Pac. J. Atmos. Sci.* **2017**, *53*, 431–443. [[CrossRef](#)]
50. University of Wyoming Home Page. Available online: <http://weather.uwyo.edu/upperair/sounding.html> (accessed on 29 January 2022).

51. CMA (China Meteorological Administration). *Specification of Routine Upper-Air Observation*; China Meteorological Press: Beijing, China, 2010; p. 58.
52. Hersbach, H.; Bell, B.; Berrisford, P.; Hirahara, S.; Horányi, A.; Muñoz-Sabater, J.; Nicolas, J.; Peubey, C.; Radu, R.; Schepers, D.; et al. The ERA5 global reanalysis. *Q. J. R. Meteorol. Soc.* **2020**, *146*, 1999–2049. [[CrossRef](#)]
53. Dee, D.P.; Uppala, S.M.; Simmons, A.J.; Berrisford, P.; Poli, P.; Kobayashi, S.; Andrae, U.; Balmaseda, M.A.; Balsamo, G.; Bauer, D.P.; et al. The ERA-Interim reanalysis: Configuration and performance of the data assimilation system. *Q. J. R. Meteorol. Soc.* **2011**, *137*, 553–597. [[CrossRef](#)]
54. Leetmaa, A.; Reynolds, R.; Jenne, R.; Joseph, D. The NCEP/NCAR 40-year reanalysis project. *Bull. Am. Meteor. Soc.* **1996**, *77*, 437–470.
55. FENGYUN Satellite Data Center Home Page. Available online: <http://satellite.nsmc.org.cn/PortalSite/Data/Satellite.aspx> (accessed on 29 January 2022).